Dimerization-Induced Cross-Layer Quasi-Two-Dimensionality in Metallic $IrTe_2$

G. L. Pascut,[1] K. Haule,[1] M. J. Gutmann,[2] S. A. Barnett,[3] A. Bombardi,[3] S. Artyukhin,[1] T. Birol,[1] D. Vanderbilt,[1] J. J. Yang,[4] S.-W. Cheong,[1,4,5] and V. Kiryukhin[1,5]

[1]*Department of Physics and Astronomy, Rutgers University, Piscataway, New Jersey 08854, USA*
[2]*ISIS Facility, STFC-Rutherford Appleton Laboratory, Didcot OX11 OQX, United Kingdom*
[3]*Diamond Light Source, Harwell Science and Innovation Campus, Didcot OX11 0DE, United Kingdom*
[4]*Laboratory of Pohang Emergent Materials and Department of Physics, Pohang University of Science and Technology, Pohang 790-784, Korea*
[5]*Rutgers Center for Emergent Materials, Rutgers University, Piscataway, New Jersey 08854, USA*

(Received 4 September 2013; revised manuscript received 22 October 2013; published 26 February 2014)

The crystal structure of layered metal $IrTe_2$ is determined using single-crystal x-ray diffraction. At $T = 220$ K, it exhibits Ir and Te dimers forming a valence-bond crystal. Electronic structure calculations reveal an intriguing quasi-two-dimensional electronic state, with planes of reduced density of states cutting diagonally through the Ir and Te layers. These planes are formed by the dimers exhibiting a signature of covalent bonding character development. Evidence for significant charge disproportionation among the dimerized and nondimerized Ir (charge order) is presented. We argue that the structural transition is driven by the Ir dimerization and bonding, while electronic correlations (dynamical mean field theory corrections to density functional theory) and spin orbit coupling play a secondary role.

DOI: 10.1103/PhysRevLett.112.086402 PACS numbers: 71.45.Lr, 61.66.Fn, 71.20.Be, 74.20.Pq

Compounds containing $5d$ electrons have been the subject of numerous recent studies. Large spin-orbit coupling combined with electron-electron interactions gives rise to many intriguing phenomena, such as a $J_{\text{eff}} = 1/2$ Mott state [1], correlated topological insulators [2], charge ordering, and ionic dimerization [3]. $IrTe_2$ is a layered chalcogenide metal composed of stacked layers of $IrTe_6$ octahedra forming a CdI_2-type structure [4] (space group $P\text{-}3m1$), see Fig. 1(a). Like many such chalcogenides, it exhibits a structural transition accompanied by a rise in the electrical resistivity, which is usually attributed to formation of a charge density wave (CDW) at low temperatures [5]. In $IrTe_2$, the structural modulation is characterized by the wave vector $q_0 = (1/5, 0, 1/5)$ with respect to the high-temperature Brillouin zone [6], and the transition temperature is $T_S \sim 280$ K [7]. Many recent experiments, however, are incompatible with the CDW description of the modulated state in $IrTe_2$, and its nature is currently under debate. For instance, a CDW gap is absent in the angle-resolved photoemission spectroscopy [8] and optical spectra [9], and the structural modulation is highly nonsinusoidal [7]. A significant role of the orbital degrees of freedom has been discussed in many recent studies, and mechanisms based on orbital-driven Peierls instability [6] or on Ir chain formation [10] have been proposed. Ir $4f$ core level x-ray photoemission experiments suggest a charge and orbital wave on the Ir sites [11]. Alternatively, a crystal field effect splitting the Te p orbitals was discussed as the driving force of the structural transition, based on optical spectroscopy experiments [9]. Depolymerization of the interlayer Te bonds was also suggested as the origin of this transition [7]. Recently, the mechanism of structural transition in $IrTe_2$ has attracted additional attention because of superconductivity in Pt-doped samples [6,10,11].

Knowledge of the crystallographic structure is necessary for understanding the modulated state in $IrTe_2$. X-ray powder diffraction for $T < T_S$ has been done, and an average monoclinic $C2/m$ structure (with unresolved atomic positions) [5] as well as a 75-atom-large triclinic unit cell [12] were reported. However, a single-crystal

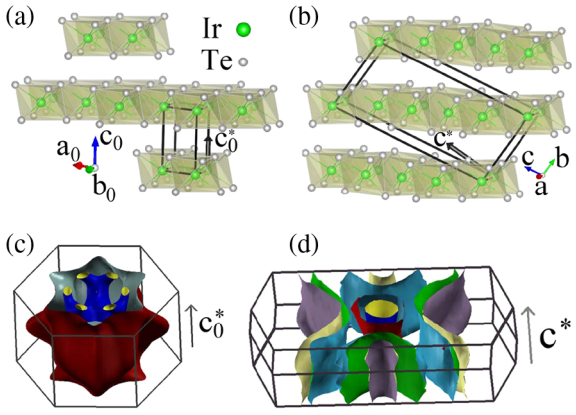

FIG. 1 (color online). The structure of $IrTe_2$ at (a) room temperature (RT) and (b) $T = 220$ K. The elementary crystallographic unit cells (boxes), axes (arrows), and reciprocal axes c_0* and $c*$ (thick arrows) are shown. Calculated Fermi surface at RT (c), and 220 K (d). At RT, the triclinic unit cell vectors a, b, c corresponding to those shown in (b) can also be introduced: $a = b_0$, $b = -a_0 - b_0 + c_0$, $c = 4a_0 + 2b_0 + c_0$. However, the triclinic cell is nonelementary at RT.

diffraction experiment is needed to determine such a complex structure reliably. Herein, we present the structure of the modulated state at $T = 220$ K determined by single-crystal x-ray diffraction. Both Ir and Te dimers form at this temperature. Electronic structure calculations provide evidence for covalent character development in the Ir dimers, as well as for charge disproportionation (charge order). The structural transition appears to be driven by the energy gain due to Ir and Te dimerization, with Ir orbitals playing a key role. Remarkably, the electronic structure of the modulated state is quasi-two-dimensional, with layers of reduced density of states at the Fermi level, formed by planes of Ir and Te dimers, cutting diagonally through the structural Ir and Te layers.

$IrTe_2$ single crystals were grown using Te flux, as described in Ref. [7]. Their bulk characteristics are consistent with the literature [6], see Fig. S1 in the Supplemental Material [13]. X-ray diffraction measurements were done at room temperature and $T = 220$ K using an Oxford Diffraction Supernova diffractometer equipped with a CCD detector and Mo K_α radiation. The room-temperature (RT) structure, shown in Fig. 1(a), is consistent with published data [4]. At $T = 220$ K, our $102 \times 33 \times 17$ μm $IrTe_2$ sample did not show any twinning (see Fig. S2 in the Supplemental Material [13]), and all the observed ~23 400 reflections were successfully indexed in the triclinic $P-1$ cell shown in Fig. 1(b). The lattice parameters are $a = 3.954\,8(2)$ Å, $b = 6.654\,2(4)$ Å, $c = 14.434\,5(7)$ Å, $\alpha = 98.129(5)°$, $\beta = 92.571(4)°$, $\gamma = 107.119(5)°$. This cell contains only eight independent atoms, allowing for a reliable structural refinement. The structure was determined from 2523 unique reflections with $F^2 > 3\sigma$; the goodness of fit was $R_1 = 0.057$. The obtained atomic coordinates, software used, and other details are given in the Supplemental Material [13].

The most remarkable feature of the $T = 220$ K structure is Ir dimerization, see Fig 2(a). The Ir dimers form stripes in the triangular Ir layers. These stripes exhibit a staircase like arrangement in the direction normal to the layers, resulting in a quintupling of the unit cell in the a_0 and c_0 directions of the high-temperature structure. The contraction of the Ir-Ir bonds in the dimers is striking—they are 20%–23% shorter than all the other bonds in the Ir layer (3.119 Å vs. 3.905–4.030 Å). In Te triangular layers, Te-Te bonds above and below the Ir dimers contract by 10%–17% compared to the other bonds (3.439 Å vs. 3.807–4.114 Å), forming similar dimerized stripes, see Fig. 2(b). Both the Ir-Ir and Te-Te in-layer distances are 3.93 Å at RT. As at high temperature, the Te-Te bonds connecting the Te layers are shorter than the nondimerized bonds in the layers due to Te polymerization. For $T = 220$ K, they show less than 6% length variation ranging from 3.385–3.582 Å (the RT value is 3.498 Å). Finally, all the Ir-Te bonds are almost equal to each other and to the RT value, and vary by less than 2%.

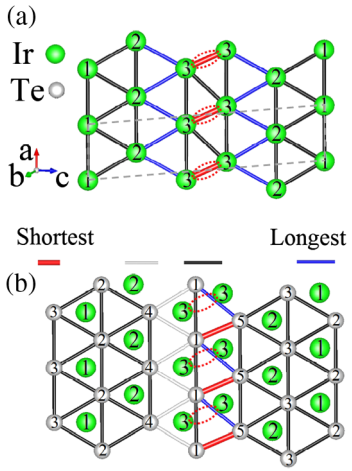

FIG. 2 (color online). (a) Triangular Ir layer at $T = 220$ K. Dashed line shows the projection of the triclinic unit cell. (b) Triangular Te layer at $T = 220$ K. The Ir layer directly above is also shown. In both panels, the bond lengths are color coded as shown in the legend, and Ir(3)-Ir(3) dimers are marked with dashed ovals.

To understand the nature of the dimerized state, we have carried out density functional theory (DFT) and dynamical mean field theory (DMFT) calculations [14] using the WIEN2K package [15], with spin-orbit coupling (SOC) fully included. The DMFT calculation was performed in the charge self-consistent implementation [16]. The energy range in computing hybridization and self-energy spanned a 20 eV window around the Fermi energy (E_F), and the values of local Coulomb repulsion $U = 4.5$ eV and Hund's coupling $J = 0.8$ eV were taken from Ref. [17]. The DFT calculations were done using the full-potential linearized augmented plane-wave basis and the GGA-PBE functional [18]. Only a minor DMFT mass enhancement for Ir $5d$ (all t_{2g}) orbitals $m*/m_{\text{band}} \sim$ 1.15–1.2 was found, indicating weak electronic correlations. The differences between the DFT and DMFT calculations were insignificant. Local total-energy minima corresponding to the high-T and low-T experimental structures were found, see Fig. S3 in the Supplemental Material [13]. The minima are separated by an energy barrier of the order of 20 meV per formula unit, consistent with a first-order phase transition. The low-T structure has a higher energy, indicating the possible importance of nonlocal interactions in the Ir dimers. Removal of SOC stabilizes the low-T state, but the calculations reproduce the local energy minima for the same structures. In all cases, the relaxed structures show very little difference with the experimental ones (less than 1% change). The local energy minimum corresponding to the dimerized structure is also preserved when the high-T trigonal unit cell vectors are used, albeit at a higher energy. These observations indicate that SOC destabilizes the dimerized state (possibly reducing the T_S), while strain effects favor the triclinic lattice distortion. The observed

dimerized structure corresponds to a local energy minimum irrespective of the presence of the SOC or unit cell deformation in the calculations. Therefore, electronic correlations (corrections to DFT), SOC, and strain do not play the primary role in the stabilization of the observed dimerized structure.

Figure 1(c) shows the calculated Fermi surface (FS) at RT; it is consistent with the published data [9]. For $T = 220$ K, the system remains metallic with the FS shown in Fig. 1(d). The key property of this FS is its marked quasi-two-dimensional (2D) character. The direction normal to the electronic 2D planes is given by the reciprocal $c*$ axis of the triclinic unit cell. This axis is normal to both the a and b triclinic axes, and at an angle of 10° to the c axis, as shown in Fig 1(b). The quasi-2D planes of the electronic structure cut diagonally through the structural Ir and Te planes. The origin of this highly unusual electronic structure, which seemingly contradicts the structural motif of the crystal lattice, is illustrated in Fig. 3. It shows that the staircaselike arrangement of the Ir and Te dimers forms a 2D "wall" centered on Ir(3)-Ir(3) dimerized bonds. This wall cuts through the Ir and Te layers in the direction normal to $c*$. As shown in Fig. 3(a), the density of states (DOS) at E_F is reduced dramatically for all the Ir and Te atoms within this wall. In contrast, only an insignificant DOS reduction is observed at E_F for the Ir and Te atoms in the 2D planes away from the dimer walls (e.g., Ir(1) and Te(2) sites). The largest DOS reduction occurs on the dimerized Ir sites. Consistently, the total DOS reduction at the E_F that takes place at the structural transition is dominated by the Ir orbitals (about 2/3 of the reduction value), as shown in Fig. 4(a).

Dimerization of Ir(3) leads to significant changes in its 5d DOS, see Fig. 4(b). The major effect is seen for the d_{xy} orbitals that overlap directly in the Ir(3)-Ir(3) dimers. (Pseudocubic axes attached to $IrTe_6$ octahedra are used, see Fig. 4(b) for a sketch of the Ir(3) d_{xy} orbitals.) Well-identified DOS peaks appear above and below E_F for these orbitals. Such peaks are absent for the other Ir(3) d orbitals (and, therefore, are less prominent in the Ir(3) total $5d$ t_{2g}

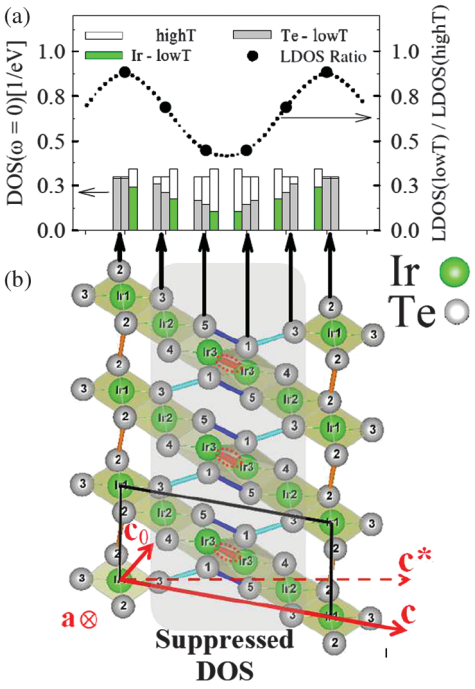

FIG 3 (color). (a) The density of states at E_F for the planes of Ir and Te atoms running normal to the $c*$ axis shown in panel (b) directly below. Each plane is identified with an arrow. The ratio of the low- (220 K-) and high- (300 K-)temperature DOS for each of these planes is also shown. (b) Projection of the $T = 220$ K structure along the triclinic a axis. The atoms form perfect columns; i.e., Ir(1) is directly below Ir(1), etc. Black box shows the projection of the unit cell. Ovals identify the Ir dimers. Shortened Te-Te bonds are shown in blue and cyan. The shaded region identifies a plane of suppressed DOS at E_F formed by Ir and Te dimers. This plane is normal to the $c*$ axis. In contrast, the structural Ir and Te layers run normal to the c_0 direction.

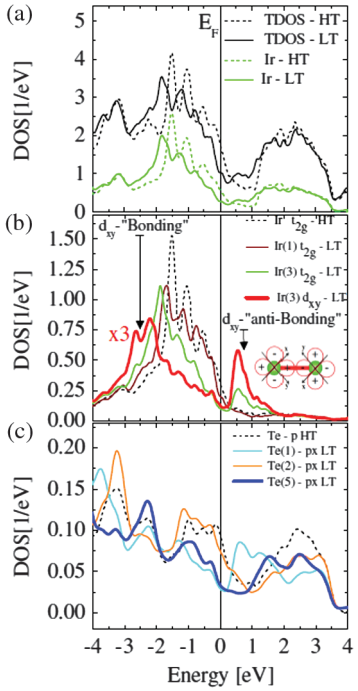

FIG. 4 (color). (a) Total density of states (TDOS), and Ir DOS at $T = 300$ K (HT) and 220 K (LT). (b) Combined DOS of the $5d$ (all t_{2g}) orbitals for Ir(1) and Ir(3) at LT, as well as for any Ir at HT. The DOS for the Ir(3) d_{xy} orbital at LT is also shown. The arrows point to the DOS peaks associated with the bonding and antibonding molecular orbitals in the Ir dimers. The corresponding antibonding orbital is sketched at right. The x, y, and z axes for the d orbitals are the local axes of the $IrTe_6$ octahedra. (c) LT DOS of the Te(1), Te(2), and Te(5) $4p_x$ orbitals for the Te(1)-Te(3), Te(2)-Te(2), and Te(5)-Te(1) bonds, respectively. The bonds are shown in Fig. 3(b) using the same color code. The x axis of each p_x orbital coincides with the corresponding Te-Te bond direction. The averaged HT Te p DOS is also shown.

DOS), for the other Ir atoms, and also at RT. Using chemistry language, they signify formation of bonding and antibonding molecular orbitals in the Ir dimers, see Fig. 4(b). These data, therefore, show evidence of covalent character development and bond formation in the Ir dimers. Ir dimerization is accompanied by a significant charge disproportionation. At RT, the total $5d$ orbital occupancy is calculated to be $n_d = 5.50$, giving formal $Ir^{3.5+}$ valence that lies in between the Ir^{4+} and Ir^{3+} states discussed in the literature [11,19]. At $T = 220$ K, $n_d = 5.22$ ($Ir^{3.78+}$) for the dimerized Ir(3), while $n_d = 5.46$ ($Ir^{3.54}$) for the other Ir atoms. In a simplified ionic description, Ir^{4+}-like Ir(3) ions form strongly bound dimers, reducing the DOS at E_F and explaining the experimentally observed drop in magnetic susceptibility [5], while the other Ir sites remain Ir^{3+}-like and form a quasi-2D subsystem with higher electric conductivity.

As shown in Fig. 3(a), the Te ions also contribute to the DOS reduction at E_F, albeit not as significantly as Ir. The changes of the DOS of the Te orbitals at T_S exhibit the same pattern as that shown by the Ir orbitals, see Fig. 4(c). The DOS at E_F is reduced significantly for the $4p$ orbitals binding the Te(1)-Te(5) dimers in the Te planes, as well as for the $4p$ orbitals in the shortest interplane Te pairs, Te (1)-Te(3). One could tentatively assign DOS peaks due to bonding and antibonding states, especially for the in-plane Te dimers, but such an interpretation is far less justified than that for the Ir(3) case. This possibly reflects the complex character of the network of Te bonds in the polymerized Te double planes, with different Te-Te bonds possessing different degrees of covalency. Outside the 2D walls of the dimerized Ir and Te, the Te p orbitals largely preserve the RT character, as shown for the Te(2)-Te(2) interplane bonds in Fig. 4(c). Since the Ir(1) $5d$ orbitals also preserve the RT character, this explains the planes of large DOS at E_F running through the network of Ir(1) and Te(2) atoms in the planes normal to $c*$.

The obtained crystallographic structure sheds a new light on previous experiments [5–12]. Our results are consistent with the reported gapless state [8,9], Ir charge order [11], and nonsinusoidal modulation [7]. The origin of the structural instability and the role of various electronic orbitals [7,9–11] are, however, reinterpreted based on the new structural data. Our electronic structure calculations reveal an unusual quasi-2D electronic state in $IrTe_2$ at low temperatures. The planes of reduced DOS at the Fermi energy consisting of dimerized Ir and Te ions cut diagonally through the triangular Ir and Te planes. These results indicate that alternating layers with higher and lower electric conductivity should run in the direction normal to the triclinic $c*$ axis in $IrTe_2$ at low temperatures. Confirmation of this prediction by either bulk or local measurements is, in our opinion, of significant interest. $IrTe_2$ can be cleaved to expose the triangular a_0b_0 plane of the high-T structure, providing an intriguing opportunity to study its quasi-2D state on an atomically flat surface running at an angle to the electronic planes. Thus, $IrTe_2$ might open a new playground for exploration of interesting surface or edge states, and uncommon domain structures. The Ir dimers exhibit evidence of covalent bonding, as well as reduced occupancy of $5d$ orbitals (Ir^{4+} character). The system can, therefore, be described using the valence-bond crystal language. As discussed above, many recent measurements argue against the Peierls instability [7–9]. This distinguishes the dimerized state in $IrTe_2$ from the low-temperature state in $CuIr_2S_4$, which also exhibits Ir^{4+}-Ir^{4+} dimers [3]. Unlike in $IrTe_2$, the latter state is insulating, the Ir^{3+}/Ir^{4+} charge order is nearly complete, and the orbitally driven Peierls mechanism is well established [20]. Spin orbit coupling destabilizes the dimerized structure in $IrTe_2$, possibly affecting T_S, while elastic strain favors the triclinic distortion. However, neither these effects nor electronic correlations are found to be the main forces driving the transition at T_S. Instead, the structural transition in $IrTe_2$ appears to be driven by Ir dimerization and bonding. Such bonding is favored in $5d$ systems with their extended electronic orbitals, and, therefore, it could be quite common in heavy-element compounds conventionally described in the framework of CDW formation.

We thank K. M. Rabe, Hongbin Zhang, C. Wilson, and T. J. Emge for fruitful discussions. This work was supported by NSF DMREF Grant No. 12-33349. G. L. P. was supported by the NSF under Grant No. DMR-1004568. The work at Postech was supported by the Max Planck POSTECH/KOREA Research Initiative Program [Grant No. 2011-0031558] through NRF of Korea funded by MEST.

[1] B. J. Kim, H. Ohsumi, T. Komesu, S. Sakai, T. Morita, H. Takagi, and T. Arima, Science **323**, 1329 (2009).
[2] Feng Lu, JianZhou Zhao, Hongming Weng, Zhong Fang, and Xi Dai, Phys. Rev. Lett. **110**, 096401 (2013).
[3] P. G. Radaelli, Y. Horibe, M. J. Gutmann, H. Ishibashi, C. H. Chen, R. M. Ibberson, Y. Koyama, Y.-S. Hor, V. Kiryukhin, and S.-W. Cheong, Nature (London) **416**, 155 (2002).
[4] S. Jobic, P. Deniard, R. Brec, J. Rouxel, A. Jouanneaux, and A. N. Fitch, Z. Anorg. Allg. Chem. **598**, 199 (1991).
[5] N. Matsumoto, K. Taniguchi, R. Endoh, H. Takano, and S. Nagata, J. Low Temp. Phys. **117**, 1129 (1999).
[6] J. J. Yang, Y. J. Choi, Y. S. Oh, A. Hogan, Y. Horibe, K. Kim, B. I. Min, and S.-W. Cheong, Phys. Rev. Lett. **108**, 116402 (2012).
[7] Y. S. Oh, J. J. Yang, Y. Horibe, and S.-W. Cheong, Phys. Rev. Lett. **110**, 127209 (2013).
[8] D. Ootsuki, S. Pyon, K. Kudo, M. Nohara, M. Horio, T. Yoshida, A. Fujimori, M. Arita, H. Anzai, H. Namatame, M. Taniguchi, N. L. Saini, and T. Mizokawa, J. Phys. Soc. Jpn. **82**, 093704 (2013).
[9] A. F. Fang, G. Xu, T. Dong, P. Zheng, and N. L. Wang, Sci. Rep. **3**, 1153 (2013).

[10] S. Pyon, K. Kudo, and M. Nohara, J. Phys. Soc. Jpn. **81**, 053701 (2012).
[11] D. Ootsuki, Y. Wakisaka, S. Pyon, K. Kudo, M. Nohara, M. Arita, H. Anzai, H. Namatame, M. Taniguchi, N. L. Saini, and T. Mizokawa, Phys. Rev. B **86**, 014519 (2012).
[12] H. Cao, B. C. Chakoumakos, X. Chen, J. Yan, M. A. McGuire, H. Yang, R. Custelcean, H. Zhou, D. J. Singh, and D. Mandrus, Phys. Rev. B **88**, 115122 (2013).
[13] See Supplemental Material at http://link.aps.org/supplemental/10.1103/PhysRevLett.112.086402 for detailed description of sample quality, x-ray experiment, and DFT calculations.
[14] G. Kotliar, S. Y. Savrasov, K. Haule, V. S. Oudovenko, O. Parcollet, and C. A. Marianetti, Rev. Mod. Phys. **78**, 865 (2006).
[15] P. Blaha, K. Schwartz, G. Madsen, D. Kvasnicka, and J. Luitz, *WIEN2k: An Augmented Plane Wave + LO Program for Calculating Crystal Properties, TU Wien, Vienna*, 2001.
[16] K. Haule, C.-H. Yee, and K. Kim, Phys. Rev. B **81**, 195107 (2010).
[17] H. Zhang, K. Haule, and D. Vanderbilt, Phys. Rev. Lett. **111**, 246402 (2013).
[18] J. P. Perdew, K. Burke, and M. Ernzerhof, Phys. Rev. Lett. **77**, 3865 (1996).
[19] S. Jobic, R. Brec, and J. Rouxel, J. Solid State Chem. **96**, 169 (1992).
[20] D. I. Khomskii and T. Mizokawa, Phys. Rev. Lett. **94**, 156402 (2005).